Diffusion of size bidisperse spheres in dense granular shear flow

Ruihuan Cai,[1] Hongyi Xiao,[2,3] Jinyang Zheng,[1] and Yongzhi Zhao[1,*]

[1]*Institute of Process Equipment, Zhejiang University, Hangzhou 310027, China*
[2]*Department of Mechanical Engineering, Northwestern University, Evanston, Illinois 60208, USA*
[3]*Department of Physics and Astronomy, University of Pennsylvania, Philadelphia, Pennsylvania 19104, USA*

Diffusion is an important particle behavior in granular flow. Although granular diffusion has been studied for decades, the diffusion of size bidisperse particles has not been well understood. In this paper, discrete element method simulations with the Lees-Edwards boundary condition are performed to quantify the relation between the diffusion coefficient (D) and flow parameters for size bidisperse spheres in dense granular flow. The influences of the shear rate ($\dot{\gamma}$), the solids fraction (f), and the diameter ratio (D_{LS}) of particles on diffusion are studied. The effects of the friction coefficient (μ) and the restitution coefficient (e) are also investigated. The results indicate that while small particles diffuse faster than large particles in a binary system the volume weighted average diffusion coefficient is proportional to the shear rate and the square of the volume weighted average particle diameter, d^2, and it is inversely proportional to the solids fraction. The quantified relation is given as $D = k_d \dot{\gamma} d^2$, where $k_d = 0.0186/f$, and this relation is not sensitive to the diameter ratio for $D_{LS} \leqslant 3$. The diffusion coefficient is not sensitive to the friction coefficient except for the extreme condition where $\mu < 0.1$, and it is also not sensitive to the restitution coefficient between 0.3 and 0.9.

I. INTRODUCTION

Diffusion is an important process relating to the fluctuation of particle motion in granular flow, which is the foundation of many thermodynamic and hydrodynamic models modified for granular systems. For granular materials, particles diffuse due to the random interactions between them, which has an important effect on macroscopic behaviors such as mixing [1,2], segregation [3–5], and rheology [6]. Diffusion has been studied extensively in various granular flows, e.g., tumbler flow [7–10], chute flow [11–13], and heap flow [2,14,15]. In addition, sheared granular system, as an important kind of granular flow where particle motions are mainly driven by external shear, has gained considerable attention [16–18] and is widely applied to diffusion studies [19–26].

Over the years, the self-diffusion of monodisperse spheres has been well understood in theory [19,22–24] and the diffusion coefficient can be obtained from experiments [25,26] and particle-based simulations [3,23,24]. Recently, the diffusion coefficient (D) of size bidisperse spheres has been studied [4,27], but still lacks systematic and quantitative characterization. For granular materials, diffusion is determined by the nature of the flow. For monodisperse spheres, in the dilute regime, where particles interact mainly through binary collision, kinetic theories [19,28] and simulation results [19] indicate $D \sim dT^{1/2}$, where d is the particle diameter and T is the granular temperature calculated based on particle velocity fluctuation. In dense monodisperse granular flow, experiments [22,25,29,30] and simulation results [3,4] indicate $D \sim \dot{\gamma} d^2$, where $\dot{\gamma}$ is the local shear rate. In quasistatic

monodisperse granular flow, the diffusion coefficient can scale as $D \sim \dot{\gamma} d^2/\sqrt{I}$, where I is the inertial number, and this is a result of collective particle behaviors [31]. Note that while typical diffusion where the mean square displacement (MSD) of particles increases linearly with time is often found, anomalous diffusion can also occur under certain conditions [32–34], which is not the focus of this paper.

For bidisperse spheres, particle diffusion in granular flow is gaining more attention due to its implications in modeling phenomena such as mixing and segregation [3–5,27,35–42]. In dense granular systems of density bidisperse spheres with equal diameter [3,35], the relation for diffusion coefficient $D \sim \dot{\gamma} d^2$ can also be obtained. In continuum models for dense granular flow of size bidisperse spheres [36–41], the diffusion coefficient is usually implemented as a constant [36,37], which can be treated as an arbitrary fitting parameter [38], obtained using empirical formulas [41], or measured directly from discrete element method (DEM) simulations [4,5,27,42]. Among these methods, determining the diffusion coefficient using DEM simulations of size bidisperse spheres in open or bounded heap flows is the most physical approach [4,5,27,42], but it still lacks enough time averaging because particles flow out of the flowing layer quickly in these systems, while diffusion is generally defined as a long-time behavior. In addition, the measurement of the diffusion coefficient in gravity driven flow can be biased by gravity-driven segregation of the two species, where large particles tend to segregate to the free surface of the flow and small particles segregate to the bottom of the flow rather than diffuse randomly. Thus, measuring the diffusion coefficient in a sheared system with no gravity-driven segregation occurring simultaneously is desirable. Previous studies have shown that the diffusion coefficient can be influenced by factors such as

*Corresponding author: yzzhao@zju.edu.cn

the particle diameter, the shear rate, the solids fraction, the friction coefficient, and the restitution coefficient [3,4,25,26]. However, investigating the individual influences of factors such as the shear rate, the particle size, and the solids fraction is hard to pursue in flow geometries including tumbler flow, chute flow, and heap flow, as these factors are always coupled in these flows and cannot be separately controlled. Similarly, the influence of the friction coefficient and the restitution coefficient also cannot be easily obtained in these flows as varying these parameters can lead to complications such as the change of repose angle and the shape and thickness of the flowing layer. Thus, it is also important to perform a systematic study in a flow geometry that allows isolating the individual influence of these factors.

In this paper, DEM simulations with the Lees-Edwards boundary condition [43] are performed to quantify the relation between the diffusion coefficient and flow parameters for size bidisperse spheres in dense granular flow. A three-dimensional (3D) cubic shear cell is simulated and a constant shear rate, independent of the solids fraction and the particle size, can be applied throughout the cell by using the Lees-Edwards boundary condition, which induces shear by moving periodic boundaries. In these simulations, there is no gravity so the measurement of diffusion is not influenced by gravity-driven segregation. The influence of the shear rate and the solids fraction is decoupled and is studied separately as they can be carefully controlled separately in each simulation. Furthermore, the influences of the particle-particle friction coefficient and the restitution coefficient are studied. The relation between the diffusion coefficient and flow parameters obtained in this paper has a clear physical meaning and it is applicable to other dense flows of size bidisperse spheres.

In Sec. II, we introduce the numerical approach including the discrete element model and simulation details. In Sec. III, we present and discuss the results of size bidisperse diffusion and the influence of various flow parameters on the scaling for the diffusion coefficient for the binary mixtures. Section IV presents a summary of this paper as well as concluding remarks. An example of applying the diffusion coefficient scaling to modeling size segregation in heap flow is presented in the Appendix.

II. SIMULATION DETAILS

A. Discrete element model

In the DEM model for spherical particles, the motion of individual particles is governed by Newton's Second Law. For a particle i with mass m_i and moment of inertia I_i, two types of particle motion are considered, translational and rotational motion, and the corresponding equations are given by

$$m_i \frac{d\boldsymbol{v}_i}{dt} = \sum_{j=1}^{n_i} \boldsymbol{F}_{c,ij}, \tag{1}$$

$$I_i \frac{d\boldsymbol{\omega}_i}{dt} = \sum_{j=1}^{n_i} \boldsymbol{T}_{c,ij}, \tag{2}$$

where $\boldsymbol{v}_i$ and $\boldsymbol{\omega}_i$ are the translational and the rotational velocity of particle i, respectively; n_i is the number of particles in contact with the particle i; $\boldsymbol{F}_{c,ij}$ and $\boldsymbol{T}_{c,ij}$ are the contact

force and the contact torque exerted on the particle i from the neighboring particle j, respectively. It should be noted that there is no gravity and no particle-wall interaction in the simulations, and only particle-particle contact force is considered.

The contact force $\boldsymbol{F}_{c,ij}$ between particle i and j is calculated by the standard soft-sphere linear spring-dashpot model [44]. $\boldsymbol{F}_{c,ij}$ consists of two components, the normal contact force $\boldsymbol{F}_{c,n,ij}$ and the tangential contact force $\boldsymbol{F}_{c,t,ij}$. They are calculated by

$$\boldsymbol{F}_{c,n,ij} = -k_n \boldsymbol{\delta}_{n,ij} - \eta_{n,ij} \boldsymbol{v}_{n,ij}, \tag{3}$$

$$\boldsymbol{F}_{c,t,ij} = -k_t \boldsymbol{\delta}_{t,ij} - \eta_{t,ij} \boldsymbol{v}_{t,ij}, \tag{4}$$

where $\boldsymbol{\delta}_{n,ij}$ and $\boldsymbol{\delta}_{t,ij}$ are the overlaps between particles in the normal and the tangential direction, respectively; $\boldsymbol{v}_{n,ij}$ and $\boldsymbol{v}_{t,ij}$ are the relative velocities of particles in the normal and the tangential direction, respectively; k_n and k_t are the normal and the tangential spring stiffness, respectively; $\eta_{n,ij}$ and $\eta_{t,ij}$ are the normal and the tangential damping, respectively, which can be calculated using the effective mass of two contact particles and the coefficient of restitution [45]. When sliding occurs between particles, i.e., $|\boldsymbol{F}_{c,t,ij}| > \mu |\boldsymbol{F}_{c,n,ij}|$, where μ is the kinetic friction coefficient, Eq. (4) is replaced by the Coulomb friction model to calculate the tangential contact force. Thus, the tangential contact force $\boldsymbol{F}_{c,t,ij}$ is then calculated by

$$\boldsymbol{F}_{c,t,ij} = -\frac{\mu |\boldsymbol{F}_{c,n,ij}| \boldsymbol{\delta}_{t,ij}}{|\boldsymbol{\delta}_{t,ij}|}. \tag{5}$$

The contact torque $\boldsymbol{T}_{c,ij}$ can be calculated by

$$\boldsymbol{T}_{c,ij} = L_{ij} \boldsymbol{n}_{ij} \times \boldsymbol{F}_{c,t,ij}, \tag{6}$$

where $\boldsymbol{n}_{ij}$ and L_{ij} represent the normal unit vector and the distance between the center of the spherical particle and the contact point, respectively.

B. Lees-Edwards boundary condition

The Lees-Edwards boundary condition is shown in Fig. 1(a). The simulation cell is surrounded by cyclic images of itself, which are the eight neighboring cells shown in Fig. 1(a). The two images aligned to the central cell in the x direction serve as streamwise periodic boundaries, while the six images in the y direction serve as moving periodic boundaries. Note that there are eight neighbor cells in a two-dimensional (2D) system and 26 neighbor cells in a 3D system for one cell. We only describe the Lees-Edwards boundary condition in a 2D system for the convenience of illustration, but it can be easily generalized to a 3D system. The simulation cell is a cube with the cell edge length equal to L. To impose a shear rate $\dot{\gamma} = U/L$, the top and the bottom moving periodic images are set in motion with velocities $U/2$ and $-U/2$ in the x direction, respectively. As shown in Fig. 1(a), when particle P exits the bottom of the simulation cell, it reenters the top of the simulation cell at P' with its velocity and location changed. Suppose the velocity and the location components of particle P in the x direction are u_P and x_P, respectively, then particle P' enters the cell with $u_{P'} = u_P + L\dot{\gamma}$ and $x_{P'} = (x_P + L\dot{\gamma} dt) \bmod L$, where mod means taking the remainder when
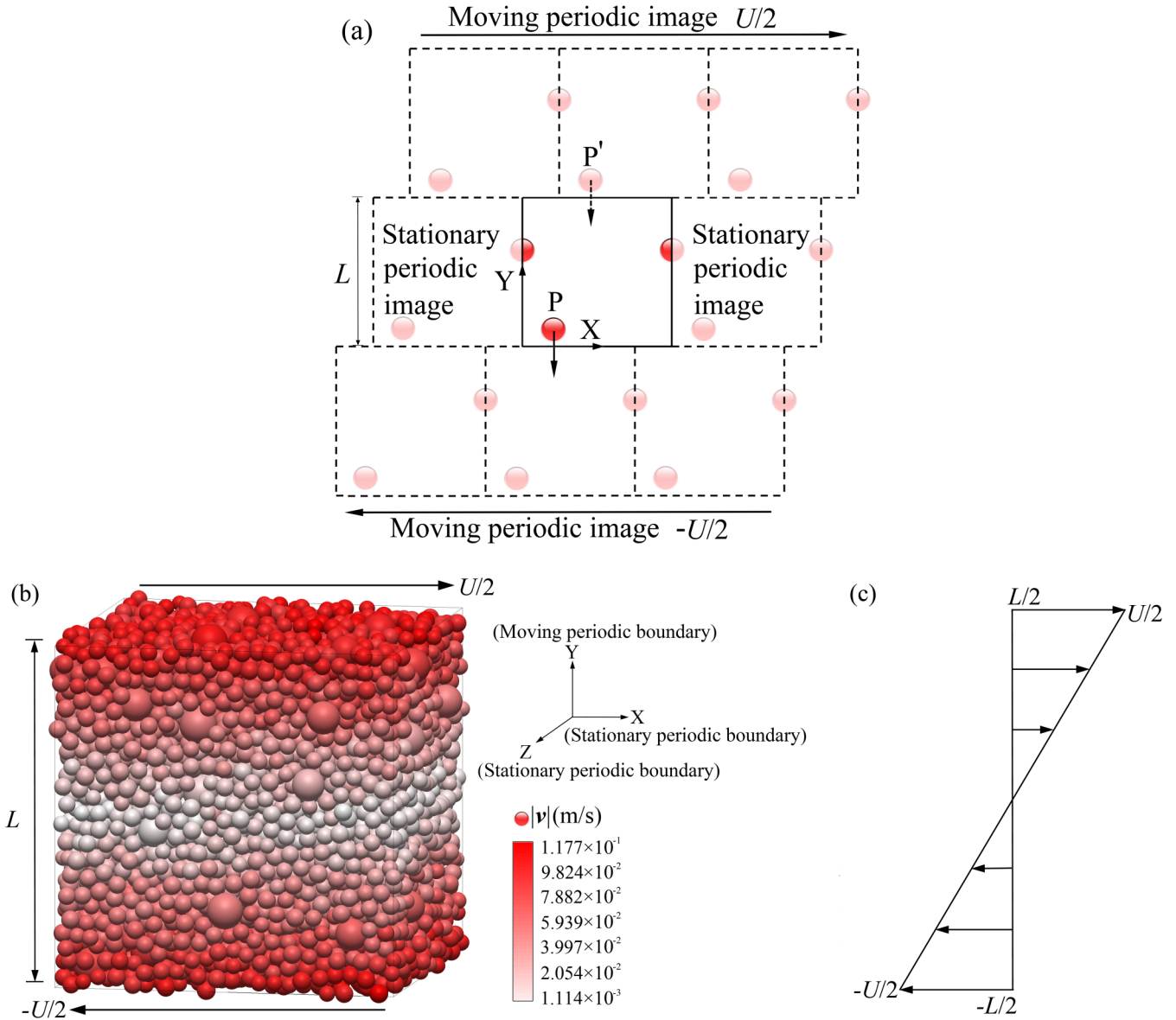
FIG. 1. Illustration of the simulation cell. (a) Lees-Edwards boundary condition. (b) Simulation cell with stationary periodic boundaries in the x and z direction and moving periodic boundaries in the y direction. Particles are colored by the magnitude of their velocity. (c) Illustration of the velocity profile in the x direction.

$(x_P + L\dot{\gamma}dt)$ is divided by L. In contrast, when the particle P exits the top of the simulation cell, it reenters the bottom of the simulation cell with $u_{P'} = u_P - L\dot{\gamma}$ and $x_{P'} = (x_P - L\dot{\gamma}t)$ mod L. In this way, a constant shear rate can be imposed throughout the simulation cell.

C. Simulation cell

We use a self-developed and previously validated DEM code [44,46,47] to perform the simulations in this paper. A simulation cell with the Lees-Edwards boundary condition in a steady state is shown in Fig. 1(b). The cell is three-dimensional with stationary periodic boundaries in the x direction as well as the z direction and moving periodic boundaries in the y direction. The cell edge length (L) is 0.02 m and the shear rate ($\dot{\gamma}$) is set to $10\,\mathrm{s}^{-1}$, resulting in the

velocity (U) of 0.2 m/s according to the relation $U = \dot{\gamma}L$. As shown in Fig. 1(b), particles are colored by the magnitude of their velocity, which shows a velocity gradient along the y direction. The velocity gradient is induced by the shear flow. Specifically, as depicted in Fig. 1(c), the velocity component in the x direction has a linear relation with the y position. Therefore, a shear flow with a constant shear rate and a uniform packing density can be obtained by this approach. Snapshots of simulations in a steady state with different diameter ratios (D_{LS}) (large to small) are shown in Fig. 2, which indicate that particles are well mixed under all size ratios throughout the simulation and size segregation does not occur.

In each simulation, two species of particles differing only in particle diameter are mixed. The particles have a constant particle density of 2600 kg/m^3. Coefficients of restitution
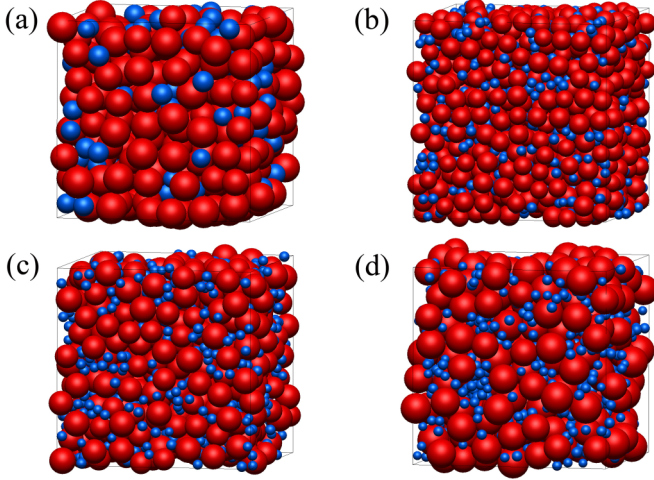
FIG. 2. Mixed state at the end of simulations for the solids fraction $f = 55\%$, the component ratio $C_{LS} = 9:1$, and the diameter ratio D_{LS} at (a) 3:2, (b) 2:1, (c) 2.5:1, and (d) 3:1. Particles are colored by the particle diameter.

TABLE II. Series of simulation conditions with different shear rates $\dot{\gamma}$ while the diameter ratio $D_{LS} = 2:1$ and the solids fraction $f = 40\%$. Note that different C_{LS} values for large spheres with $d_{\text{single}} = 2$ mm and small spheres with $d_{\text{single}} = 1$ mm result in d^2 varying from 1.21 to 3.61 mm^2.

D_{LS}	d^2 (mm^2)	C_{LS}	$\dot{\gamma}$ (s^{-1})
2:1	1.21	1:9	0, 1, 5, 10, 100
2:1	1.44	2:8	0, 1, 5, 10, 100
2:1	1.69	3:7	0, 1, 5, 10, 100
2:1	1.96	4:6	0, 1, 5, 10, 100
2:1	2.25	5:5	0, 1, 5, 10, 100
2:1	2.56	6:4	0, 1, 5, 10, 100
2:1	2.89	7:3	0, 1, 5, 10, 100
2:1	3.24	8:2	0, 1, 5, 10, 100
2:1	3.61	9:1	0, 1, 5, 10, 100

and friction are 0.9 and 0.3, respectively, unless otherwise specified. The time step is set to be smaller than $\Delta t = t_c/10$, according to Ting and Corkum [45], where t_c is the binary collision time. Thus, an integration time step of 5×10^{-6} s is adopted in this paper. To prevent particle ordering, particle diameters are uniformly distributed within $0.9d_{\text{single}}$ and $1.1d_{\text{single}}$, where d_{single} is the average particle diameter for a single species. Parameters of the simulations are summarized in Table I. Note that the average particle diameter d in each simulation is calculated by the weighted volume of particles and given by

$$d = \frac{\sum_{i=1}^{n} d_i V_i}{\sum_{i=1}^{n} V_i}, \qquad (7)$$

where d_i and V_i are the diameter and the volume of particle i; n is the number of the total particles in the simulation cell.

To investigate the relation between the diffusion coefficient and related flow parameters, e.g., the shear rate ($\dot{\gamma}$), the solids fraction (f), and the diameter ratio (D_{LS}) (large to small),

etc., simulations systematically varying these parameters are conducted. First, the effect of different shear rates at 0, 1, 5, 10, and 100 s^{-1} is studied. The simulation conditions with different shear rates while the diameter ratio $D_{LS} = 2:1$ and the solids fraction $f = 40\%$ are presented in Table II. Different component ratios (C_{LS}) (large to small by volume) from 1:9 to 9:1 result in d^2 ranging from 1.21 to 3.61 mm^2. Then, the effect of the diameter ratio and the solids fraction is studied. The simulation parameters in 44 cases with four diameter ratios, i.e., $D_{LS} = 3:2$, 2:1, 2.5:1, and 3:1, and 11 component ratios C_{LS} from 0:10 to 10:0 are shown in Table III while the shear rate $\dot{\gamma} = 10$ s^{-1} and the solids fraction $f = 40\%$. We also perform the same 44 simulations to investigate the effect of the solids fraction in dense flow, with f set to 45, 50, and 55%.

In addition, the influences of the friction and the restitution coefficients (μ and e) are also studied using 99 simulations with the friction coefficient μ varying from 0 to 1 while the restitution coefficient is fixed to $e = 0.9$, and 63 simulations with the restitution coefficient e varying from 0.3 to 0.9 while the friction coefficient is fixed to $\mu = 0.3$. The parameters used in these simulations are summarized in Tables IV and V, respectively.

III. RESULTS AND DISCUSSIONS

A. Diffusion coefficient of size bidisperse spheres

The diffusion coefficient is obtained by tracking particle trajectories and calculating the MSD of particles. In this paper, we only consider diffusion in the y direction, i.e., the direction perpendicular to the shear flow, since it is the relevant direction for processes such as segregation. The MSD in the y direction is calculated as $\langle \Delta y(\Delta t)^2 \rangle$, where $\langle \rangle$ represents averaging over all particles. Note that for calculating the MSD for the mixture the contribution of the square displacement of each particle to the total square displacement is weighted by the particle volume, as larger particles take up a larger volume of the simulation cell. The displacement of each particle within Δt is given as

$$\Delta y(\Delta t) = y(t_0 + \Delta t) - y(t_0) - \int_{t_0}^{t_0 + \Delta t} v(t)\,dt, \qquad (8)$$

TABLE I. Parameter variables and values used in the simulations.

Parameters	Values
Simulation cell edge, L (m)	0.02
Shear rate, $\dot{\gamma}$ (s^{-1})	1, 5, 10, 100
Solids fraction, f	40, 45, 50, 55%
Diameter ratio of particles, D_{LS} (large to small)	3:2, 2:1, 2.5:1, 3:1
Component ratio of particles, C_{LS} (large to small)	0:10, 1:9, 2:8, …, 10:0
Average particle diameter, d (mm)	
Particle shape	Spherical
Particle diameter, d_{single} (mm)	1, 2, 2.5, 3
Coefficient of restitution, e	0.3, 0.4, 0.5, …, 0.9
Coefficient of friction, μ	0, 0.1, 0.2, …, 0.9, 1
Time steps (s)	5×10^{-6}

TABLE III. Series of simulation conditions with different diameter ratios D_{LS} and different component ratios C_{LS} when the shear rate $\dot{\gamma} = 10\ \text{s}^{-1}$ and the solids fraction $f = 40\%$. Note that when $D_{LS} = 2{:}1$ different C_{LS} values for large spheres with $d_{\text{single}} = 2\,\text{mm}$ and small spheres with $d_{\text{single}} = 1\text{mm}$ result in d^2 varying from 1.21 to 3.61 mm^2. d^2 can be obtained in the same way for systems with $D_{LS} = 3 : 2$, 2.5:1, and 3:1.

D_{LS}	d^2 (mm^2)	C_{LS}	D_{LS}	d^2 (mm^2)	C_{LS}	D_{LS}	d^2 (mm^2)	C_{LS}	D_{LS}	d^2 (mm^2)	C_{LS}
3:2	4.00	0:10	2:1	1.00	0:10	2.5:1	1.00	0:10	3:1	1.00	0:10
3:2	4.42	1:9	2:1	1.21	1:9	2.5:1	1.32	1:9	3:1	1.45	1:9
3:2	4.85	2:8	2:1	1.44	2:8	2.5:1	1.70	2:8	3:1	1.97	2:8
3:2	5.29	3:7	2:1	1.69	3:7	2.5:1	2.11	3:7	3:1	2.56	3:7
3:2	5.76	4:6	2:1	1.96	4:6	2.5:1	2.56	4:6	3:1	3.25	4:6
3:2	6.26	5:5	2:1	2.25	5:5	2.5:1	3.07	5:5	3:1	4.01	5:5
3:2	6.76	6:4	2:1	2.56	6:4	2.5:1	3.61	6:4	3:1	4.84	6:4
3:2	7.29	7:3	2:1	2.89	7:3	2.5:1	4.20	7:3	3:1	5.77	7:3
3:2	7.84	8:2	2:1	3.24	8:2	2.5:1	4.84	8:2	3:1	6.77	8:2
3:2	8.41	9:1	2:1	3.61	9:1	2.5:1	5.52	9:1	3:1	7.84	9:1
3:2	9.00	10:0	2:1	4.00	10:0	2.5:1	6.25	10:0	3:1	9.00	10:0

where t_0 is the initial time and Δt is an arbitrary time interval; y is the particle location in the y direction (note that y is the actual location in an infinite space rather than in the simulation cell); $v(t)$ is the average velocity of all particles in the simulation cell in the y direction. In the simulations, the average velocity of all particles in the y direction is approximately zero with a small degree of random fluctuation. The diffusion coefficient D can be obtained by

$$\langle \Delta y^2 \rangle = 2D\Delta t. \tag{9}$$

Figure 3 shows an example of the MSD versus time in the y direction for a simulation with $D_{LS} = 2{:}1$, $C_{LS} = 2{:}8$, $f = 40\%$, and $\dot{\gamma} = 10\,\text{s}^{-1}$. The volume weighted average MSD for the mixture and the MSD for each individual species are shown. The results indicate that there are two regimes for each curve. For $t < 2\,\text{s}$, the particles are superdiffusive while the flow undergoes small shear deformation, which is evident by the anomalous diffusion exponent between 1 and 2 [34,48]. For $t > 2\,\text{s}$, a normal diffusive behavior is observed with the MSD increasing approximately linearly with time, consistent with previous observations [25,27,31,48], The MSD of each

individual species also increases approximately linearly with time, which is similar to the average MSD. However, Fig. 3 shows that the MSDs for small particles are larger than the MSDs for large particles, indicating that the small particles are diffusing faster than the large particles in a binary mixture. After obtaining the MSD, diffusion coefficient D can be calculated by Eq. (9). In each case, D is calculated for the mixture and for each individual species by linear fittings of the linear portions in the MSD profiles ($t > 2\,\text{s}$ for the case in Fig. 3). Note that in Fig. 3 the fitted power law exponent for this portion is slightly below 1, and we neglect this small non-linearity and assume linearity when measuring the diffusion coefficient, as was done in previous studies [25,27,31,48].

B. Diffusion coefficient versus shear rate

Diffusive motion of particles requires random collisions and void generations, which is mainly induced by shear. Thus, the diffusion coefficient D has a strong dependence on the shear rate $\dot{\gamma}$ [23,25,26]. The relation between the diffusion coefficient and the shear rate with the diameter ratio $D_{LS} = 2{:}1$ and the solids fraction $f = 40\%$ is shown in

TABLE IV. Series of simulation conditions with the friction coefficient μ varying from 0 to 1 and the restitution coefficient $e = 0.9$ when the shear rate $\dot{\gamma} = 10\ \text{s}^{-1}$, the diameter ratio $D_{LS} = 2{:}1$, and the solids fraction $f = 40\%$. Note that different C_{LS} values for large spheres with $d_{\text{single}} = 2\,\text{mm}$ and small spheres with $d_{\text{single}} = 1\text{mm}$ result in d^2 varying from 1.21 to 3.61 mm^2.

D_{LS}	d^2 (mm^2)	C_{LS}	μ	e
2:1	1.21	1:9	0, 0.1, 0.2, …, 0.9, 1	0.9
2:1	1.44	2:8	0, 0.1, 0.2, …, 0.9, 1	0.9
2:1	1.69	3:7	0, 0.1, 0.2, …, 0.9, 1	0.9
2:1	1.96	4:6	0, 0.1, 0.2, …, 0.9, 1	0.9
2:1	2.25	5:5	0, 0.1, 0.2, …, 0.9, 1	0.9
2:1	2.56	6:4	0, 0.1, 0.2, …, 0.9, 1	0.9
2:1	2.89	7:3	0, 0.1, 0.2, …, 0.9, 1	0.9
2:1	3.24	8:2	0, 0.1, 0.2, …, 0.9, 1	0.9
2:1	3.61	9:1	0, 0.1, 0.2, …, 0.9, 1	0.9

TABLE V. Series of simulation conditions with the restitution coefficient e varying from 0.3 to 0.9 and the friction coefficient $\mu = 0.3$ when the shear rate $\dot{\gamma} = 10\ \text{s}^{-1}$, the diameter ratio $D_{LS} = 2{:}1$, and the solids fraction $f = 40\%$. Note that different C_{LS} values for large spheres with $d_{\text{single}} = 2\,\text{mm}$ and small spheres with $d_{\text{single}} = 1\,\text{mm}$ result in d^2 varying from 1.21 to 3.61 mm^2.

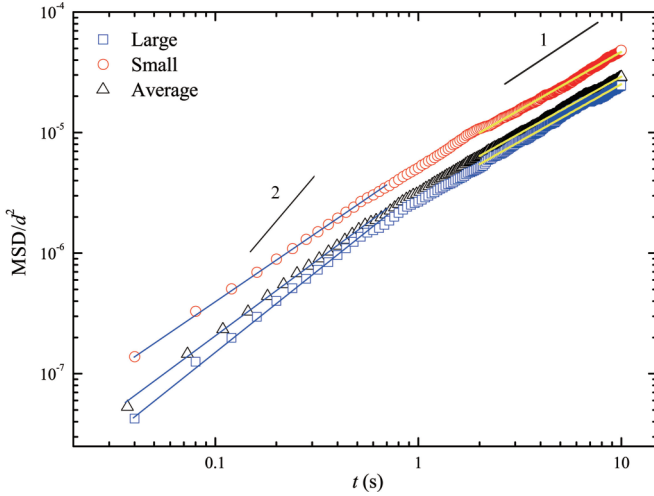| D_{LS}	d^2 (mm^2)	C_{LS}	μ	e
2:1	1.21	1:9	0.3	0.3, 0.4, 0.5, …, 0.9
2:1	1.44	2:8	0.3	0.3, 0.4, 0.5, …, 0.9
2:1	1.69	3:7	0.3	0.3, 0.4, 0.5, …, 0.9
2:1	1.96	4:6	0.3	0.3, 0.4, 0.5, …, 0.9
2:1	2.25	5:5	0.3	0.3, 0.4, 0.5, …, 0.9
2:1	2.56	6:4	0.3	0.3, 0.4, 0.5, …, 0.9
2:1	2.89	7:3	0.3	0.3, 0.4, 0.5, …, 0.9
2:1	3.24	8:2	0.3	0.3, 0.4, 0.5, …, 0.9
2:1	3.61	9:1	0.3	0.3, 0.4, 0.5, …, 0.9

FIG. 3. MSD vs time for the diameter ratio $D_{LS} = 2:1$, the component ratio $C_{LS} = 2:8$, the solids fraction $f = 40\%$, and the shear rate $\dot{\gamma} = 10\,\text{s}^{-1}$. Blue lines are power law fits to the data sets for the duration from 0 to 0.7 s, with fitted exponents of 1.13, 1.24, and 1.29 for small (red circles), average (black triangles), and large (blue squares), respectively. Yellow lines are power law fits to the data sets for the duration from 2 to 10 s, with fitted exponents of 0.96, 0.94, and 0.95 for small (red circles), average (black triangles), and large (blue squares), respectively.

Fig. 4. Nine symbols represent nine squares of the average particle diameter, d^2, which is obtained by changing particle component ratio C_{LS}, and the simulation parameters are shown in Table II. Note that, different from the particle diameter for monodisperse spheres, d here is a variable representing the average particle diameter calculated by Eq. (7). As shown in Fig. 4(a), for each d^2 (i.e., each C_{LS}), the average diffusion coefficient of the mixture increases linearly with the shear rate. For a closer examination, an enlarged view with $\dot{\gamma}$ varying from 0 to $10\,\text{s}^{-1}$ is shown in the inset of Fig. 4(a), which also indicates that the average diffusion coefficient is linear to the shear rate, i.e., $D \sim \dot{\gamma}$. The diffusion coefficient for each individual species versus the shear rate is also shown in Figs. 4(b) and 4(c), which indicates the same scaling, i.e., $D \sim \dot{\gamma}$. Note that although we are plotting the linear fitting starting from zero shear rate this linear relation may not hold for extremely low shear rates [27,31], which are not examined in this paper. The results in Figs. 4(b) and 4(c) show that in a size bidisperse mixture the diffusion coefficient of the small particles is larger than the diffusion coefficient of the large particles, which is consistent with the observation of the MSD difference in Fig. 3. This trend will be made clear in the following subsection.

C. Diffusion coefficient versus particle size

Previous studies in size monodisperse flows indicated that the diffusion coefficient D is also proportional to the square of the particle diameter [3,4,22,25,29,30]. Recent studies [4,27] indicate that this relation is still feasible in bidisperse granular flow with the diameter being the volume (concentration) weighted average diameter. Therefore, we replot the
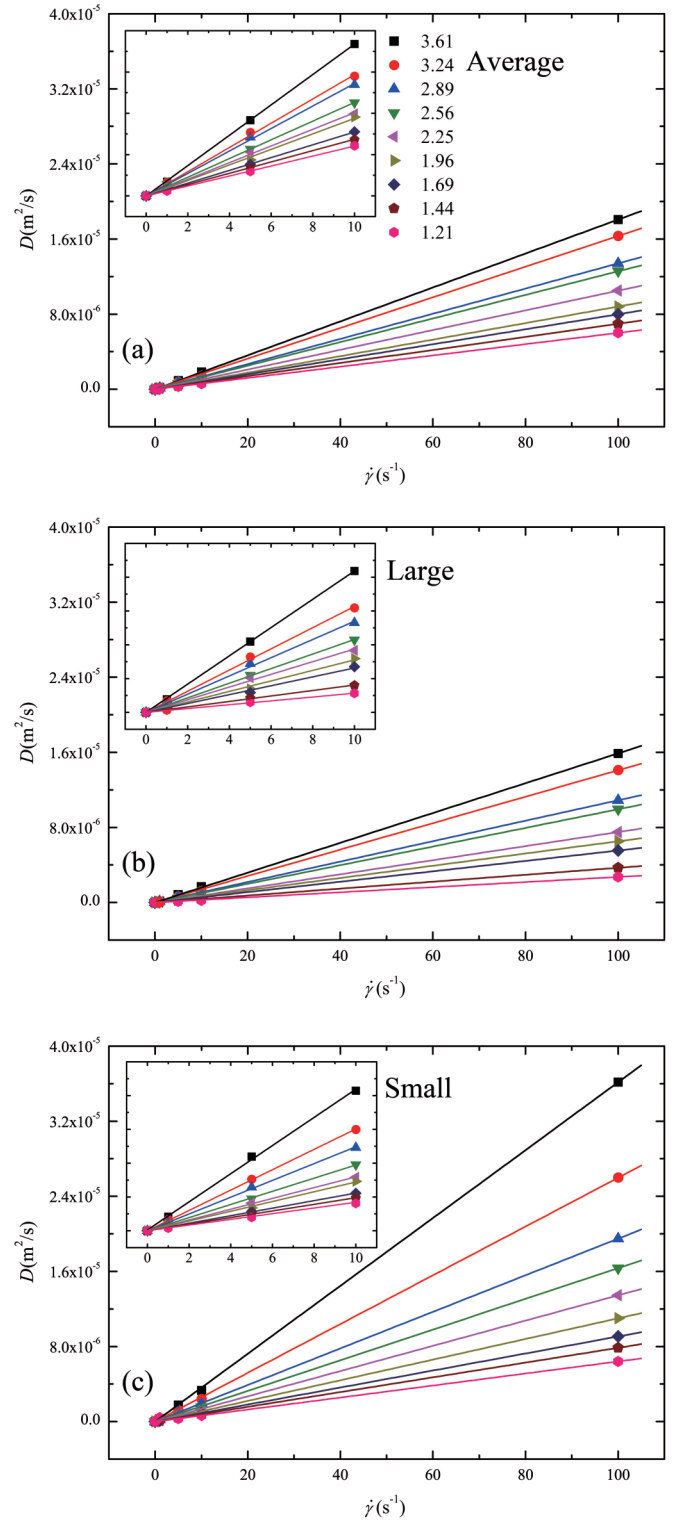

FIG. 4. The diffusion coefficient D vs the shear rate $\dot{\gamma}$ for $\dot{\gamma}$ at 0, 1, 5, 10, and $100\,\text{s}^{-1}$ with the diameter ratio $D_{LS} = 2:1$, the solids fraction $f = 40\%$, and d^2 ranging from 1.21 to $3.61\,\text{mm}^2$ achieved by changing the component ratio C_{LS}. (a) The average diffusion coefficient vs the shear rate. (b) The diffusion coefficient of large spheres vs the shear rate. (c) The diffusion coefficient of small spheres vs the shear rate. The straight lines are linear fittings to data.
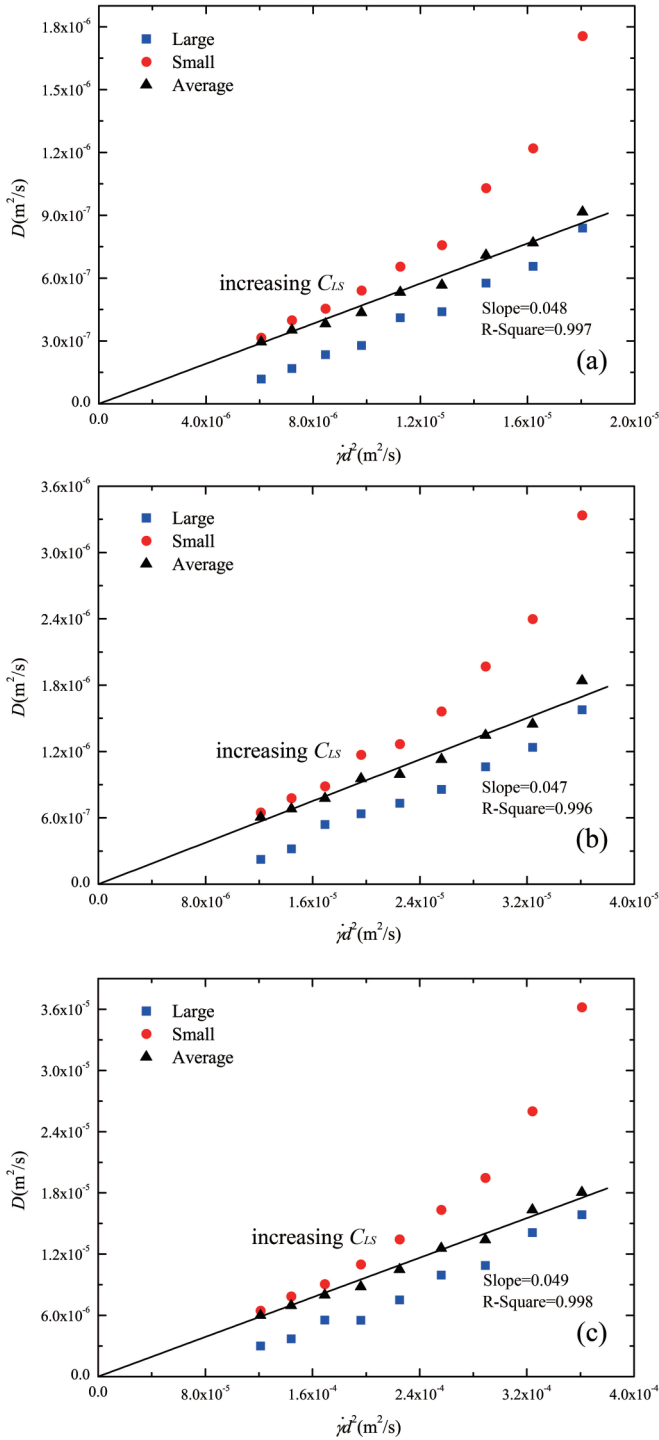
FIG. 5. The average diffusion coefficient D (black triangles) vs $\dot{\gamma}d^2$ with changing the component ratio C_{LS} for the shear rate (a) $\dot{\gamma} = 5\,\text{s}^{-1}$, (b) $\dot{\gamma} = 10\,\text{s}^{-1}$, and (c) $\dot{\gamma} = 100\,\text{s}^{-1}$. The diffusion coefficient for each individual species (red circles for small, blue squares for large) is also shown in panels (a)–(c). The black lines are linear fits to the average diffusion coefficient D vs $\dot{\gamma}d^2$.

data (from Fig. 4) by showing D versus $\dot{\gamma}d^2$ at different d^2 achieved by varying component ratio C_{LS} for a mixture with the diameter ratio $D_{LS} = 2{:}1$ and the solids fraction $f = 40\%$ in Figs. 5(a)–5(c). Each subfigure shows data with a constant

shear rate at 5, 10, and $100\,\text{s}^{-1}$, respectively. The diffusion coefficient for each individual species is also shown along with the average diffusion coefficient. Under all three shear rates, the results show that the small particles have larger diffusion coefficients at all d^2. This further confirms that in bidisperse mixtures small particles diffuse faster than large particles. While the scaling for the diffusion coefficient of each individual species is not clear, a linear relation between the average diffusion coefficient and the square of the average particle diameter d^2 is shown in Figs. 5(a)–5(c), which justifies using the volume (concentration) weighted average diameter to scale the average diffusion coefficient of the mixture, $D \sim \dot{\gamma}d^2$, in previous studies [4,27].

The difference between the diffusivity of small and large particles in a binary mixture is intriguing, because for diffusion of monodisperse spheres the scaling $D \sim \dot{\gamma}d^2$ suggests that larger particles should have larger diffusion coefficients, which is clearly not the case for the individual species in a mixture. In Figs. 5(a)–5(c), at small d^2 (small C_{LS}), the average diffusion coefficient is close to that of small particles, as the simulation cell is dominated by small particles by volume, and the few large particles in the cell diffuse slower than average. At large d^2 (large C_{LS}), the average diffusion coefficient is close to that of large particles, as the simulation cell is dominated by large particles by volume, and the few small particles in the cell diffuse faster than average. The ratio between the diffusion coefficients of the two species and the rate of increase of the diffusion coefficient of the two species with d^2 appear to be concentration dependent. This is reminiscent of the concentration effect on the asymmetry of the segregation phenomenon observed in previous studies, where a few small particles in a large particle dominated flow have much greater segregation velocity than a few large particles in a small particle dominated flow, and the relation between the segregation velocity and concentration is nonlinear [49,50]. The connection between these two phenomena should be investigated in future studies.

D. Diffusion coefficient versus solids fraction

The results above systematically show that the diffusion coefficient scales as $D \sim \dot{\gamma}d^2$ in dense granular flow of size bidisperse spheres. To quantify this relation, a constant k_d is introduced, which is determined by the slope of the linear fit for the relation between D and $\dot{\gamma}d^2$. In this way, the relation can be expressed as $D = k_d\dot{\gamma}d^2$. Previous studies in monodisperse flows indicated that the diffusion coefficient decreases as the solids fraction increases [23,26]. In this subsection, we quantitatively examine the influence of the solids fraction on the relation for the diffusion coefficient. We choose four solids fractions, 40, 45, 50, and 55%, for investigating size bidisperse diffusion. A solids fraction below 40% is not considered as we do not focus on the dilute regime where different diffusion behavior can occur [23].

Figure 6 presents the measured diffusion coefficient versus $\dot{\gamma}d^2$ with the solids fraction f set to 40, 45, 50, and 55%, and with the diameter ratio D_{LS} set to 3:2, 2:1, 2.5:1, and 3:1. The simulation conditions are shown in Table II. As shown in Fig. 6, the data in each set of simulations with a fixed solids fraction confirm the relation $D = k_d\dot{\gamma}d^2$. However, for
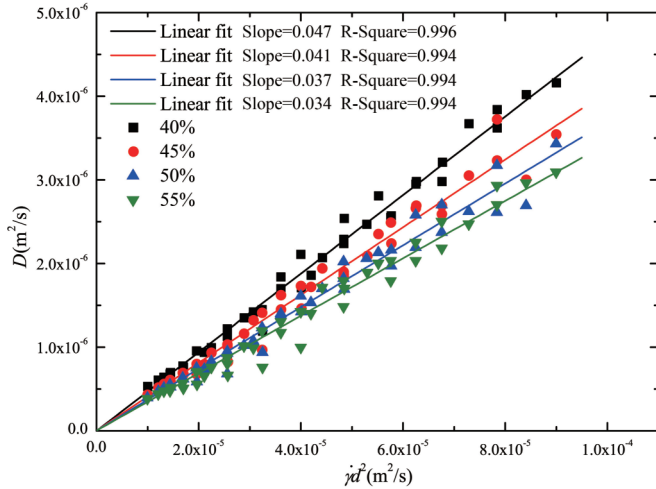
FIG. 6. The diffusion coefficient D vs $\dot{\gamma} d^2$ with the solids fraction f being 40, 45, 50, and 55%. The data points for each solids fraction include simulations with the diameter ratio D_{LS} being 3:2, 2:1, 2.5:1, and 3:1.

simulations with different solids fractions, the results show that the diffusion coefficient increases as the solids fraction decreases, similar to the results in monodisperse granular flows [23]. This means that k_d increases as the solids fraction decreases, which is evident by the different slopes in Fig. 6. To better understand the dependence of diffusion on the solids fraction for size bidisperse spheres, the relation between k_d and f is shown in Fig. 7. The results confirm that k_d decreases as f increases, and this relation can be approximated to the first order by $k_d \sim 1/f$. Figure 7 also shows that k_d is not sensitive to the diameter ratio.

E. Scaling of the diffusion coefficient

The relation between k_d and f suggests that the diffusion coefficient should scale with $1/f$. To demonstrate this scaling, the diffusion coefficient normalized by the solids fraction is
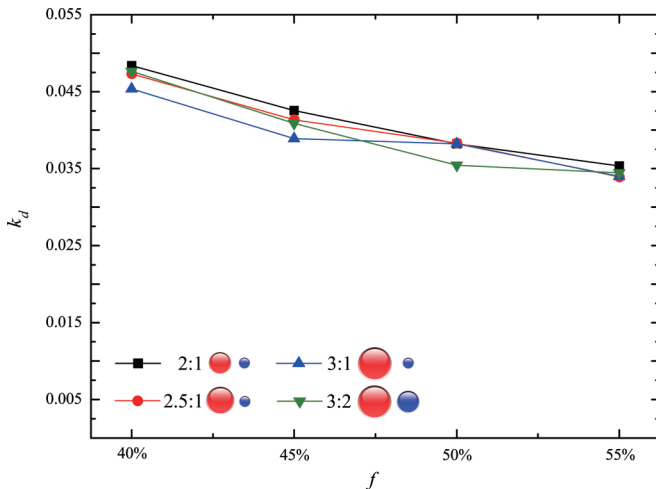

FIG. 7. k_d vs the solids fraction f with f at 40, 45, 50, and 55%, and the diameter ratio D_{LS} at 3:2 (inverted green triangles), 2:1 (black squares), 2.5:1 (red circles), and 3:1 (blue triangles).
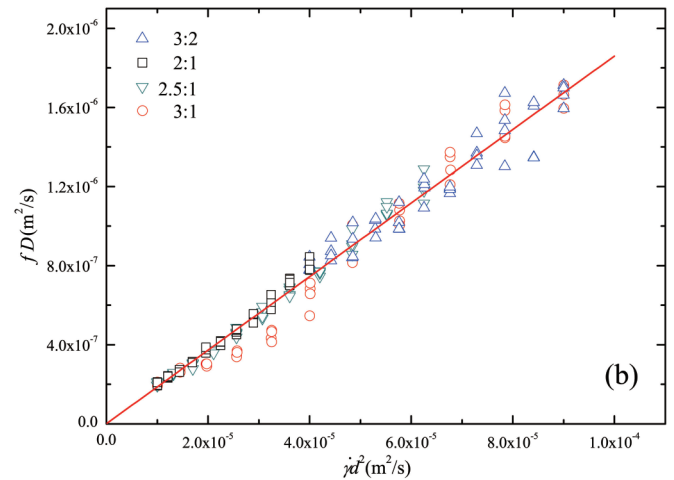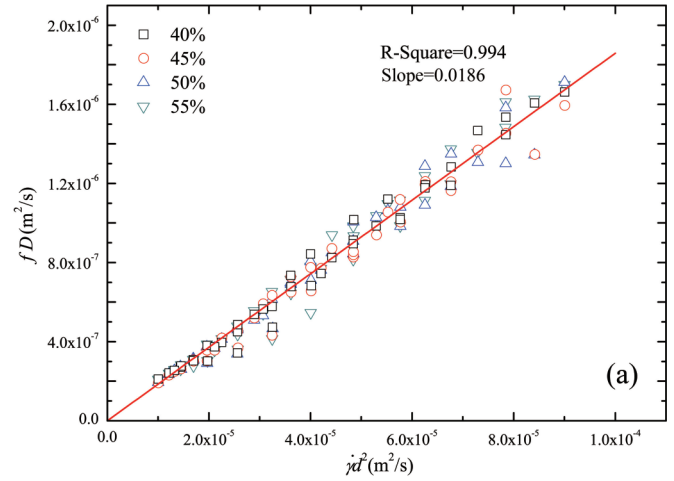

FIG. 8. fD vs $\dot{\gamma} d^2$ for the shear rate $\dot{\gamma} = 10\,\mathrm{s}^{-1}$. The data are marked by (a) the solids fraction f varying from 40 to 55% and (b) the diameter ratio D_{LS} varying from 3:2 to 3:1. The red solid line is the linear fit to fD vs $\dot{\gamma} d^2$.

shown in Fig. 8(a), which shows that all the data points collapse onto a single line, indicating that $D \sim 1/f$. To include the influence of the solids fraction, the diffusion coefficient is thus expressed as

$$D = k_d \dot{\gamma} d^2, \tag{10}$$

where k_d is the slope for D versus $\dot{\gamma} d^2$, which is dependent on the solids fraction

$$k_d = \frac{k_D}{f}, \tag{11}$$

where k_d is the slope of the fitted line for the dependence of fD on $\dot{\gamma} d^2$, as shown in Fig. 8(a), with the value $k_D = 0.0186$, which is fitted from data from 176 simulations with the diameter ratio D_{LS} varying from 3:2 to 3:1, the component ratio C_{LS} varying from 0:10 to 10:0, and the solids fraction f varying from 40 to 55%. Here, we prefer to use the solids fraction f in the scaling, because f is the parameter that is directly set in the simulations. For pressure-controlled systems, it might be of interest to express f as a function of the inertial number I, following the approach in Ref. [51], although a recent
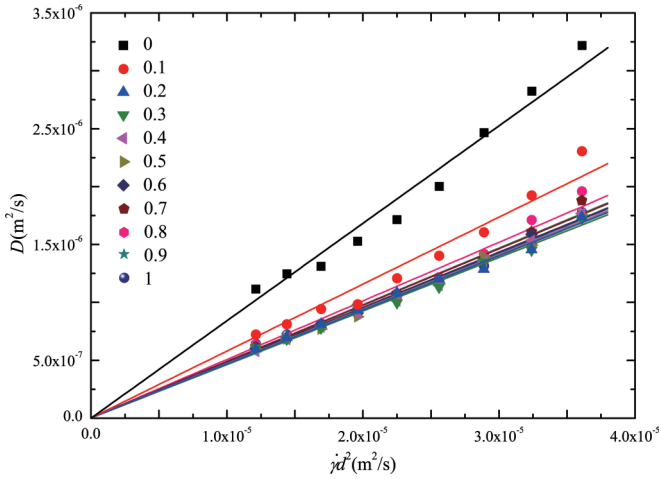
FIG. 9. The diffusion coefficient D vs $\dot{\gamma}d^2$ with the friction coefficient μ varying from 0 to 1, while the shear rate $\dot{\gamma} = 10\,\mathrm{s}^{-1}$, the diameter ratio $D_{LS} = 2{:}1$, the solids fraction $f = 40\%$, and the restitution coefficient $e = 0.9$. The straight lines are linear fittings to data.

study indicates that the diffusion process is insensitive to the pressure [52].

While most of the data collapse in Fig. 8(a), it is clear that a few data points are not collapsing well. To understand where the scatter comes from, we replot the data in Fig. 8(b) with the data marked by the diameter ratio, and we find that there is a relatively larger scatter for the data with $D_{LS} = 3{:}1$. This indicates that a larger diameter ratio D_{LS} is more likely to incur scatter, although k_d stays constant for different diameter ratios, as shown in Fig. 7. This indicates a possibility that the diffusion behavior with extremely large particle size ratio ($D_{LS} > 3$) can be different. However, the slight scatter hardly affects the accuracy of the quantified relation.

F. Effects of the friction coefficient

The particle-particle friction coefficient can influence the behavior of granular flow [53,54]. To investigate the influence of the friction coefficient on diffusion, we plot the diffusion coefficient versus $\dot{\gamma}d^2$ in Fig. 9 with the friction coefficient μ varied from 0 to 1 while the other simulation parameters held fixed at $\dot{\gamma} = 10\,\mathrm{s}^{-1}$, $D_{LS} = 2{:}1$, $f = 40\%$, and $e = 0.9$. For each friction coefficient, we performed a group of simulations varying the component ratio C_{LS}, and the simulation condition is summarized in Table IV. Figure 9 demonstrates that the diffusion coefficient is not sensitive to the friction coefficient for $\mu > 0.1$, indicating that for commonly used frictional particles the influence of the friction coefficient is negligible, and k_d can be considered as a constant as measured in Eq. (10). However, for $\mu < 0.1$, the diffusion coefficient significantly increases with decreasing the friction coefficient. The case with $\mu = 0$ is a condition where the particles are perfectly smooth without any rotational motion, and the k_d measured in this set of data is significantly larger. For the increase of the diffusion coefficient with decreasing μ when $\mu < 0.1$, we speculate that this increase is related to the reduced rotational motion, as the translational and the rotational motion are coupled by friction [54] and particle diffusion is a result of
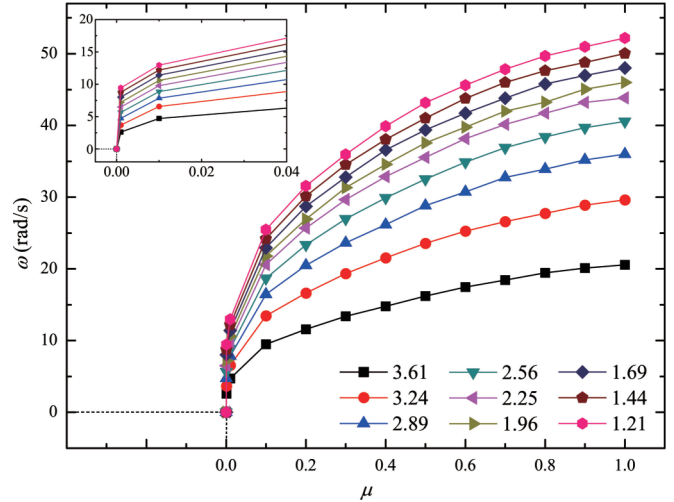

FIG. 10. The rotation velocity ω vs the friction coefficient μ with μ varying from 0 to 1, while the shear rate $\dot{\gamma} = 10\,\mathrm{s}^{-1}$, the diameter ratio $D_{LS} = 2{:}1$, the solids fraction $f = 40\%$, and the restitution coefficient $e = 0.9$. Inset: Enlarged view with μ near zero ($\mu = 0, 0.001,$ and 0.01) .

the translational motion. Thus, the rotational motion is studied in each simulation to further investigate this coupling and we calculate the average rotational velocity weighted by particle volume. The average rotational velocity ω versus the friction coefficient with μ varying from 0 to 1 is shown in Fig. 10. The result shows that there is a relatively sharp increase between $\mu = 0$ and 0.1, which is made clear by the inset of Fig. 10. This corresponds well with the change in diffusion in Fig. 9.

G. Effects of the restitution coefficient

The diffusion coefficient versus $\dot{\gamma}d^2$ is shown in Fig. 11 with the restitution coefficient e varying from 0.3 to 0.9 with $\dot{\gamma} = 10\,s^{-1}$, $D_{LS} = 2{:}1$, $f = 40\%$, and $\mu = 0.3$. The simulation condition is summarized in Table V. In Fig. 11, a larger
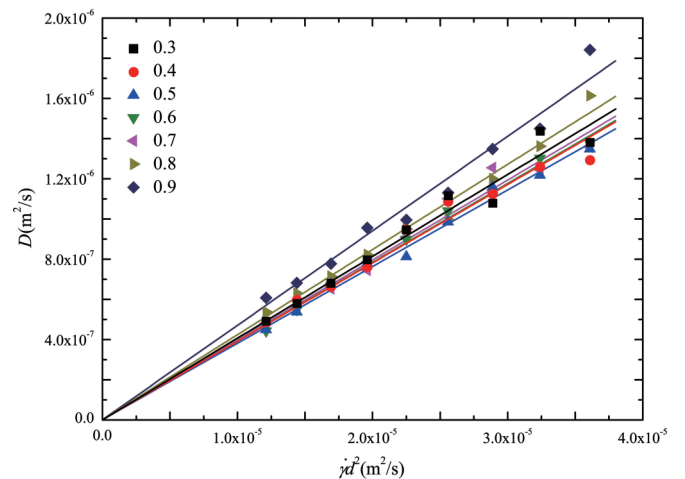

FIG. 11. The diffusion coefficient D vs $\dot{\gamma}d^2$ with the restitution coefficient e varying from 0.3 to 0.9 while the shear rate $\dot{\gamma} = 10\,\mathrm{s}^{-1}$, the diameter ratio $D_{LS} = 2{:}1$, the solids fraction $f = 40\%$, and the friction coefficient $\mu = 0.3$. The straight lines are linear fittings to data.

restitution coefficient results in a slightly larger diffusion coefficient, but in general, in the dense regime, the diffusion coefficient is not very sensitive to the restitution coefficient. Consequently, this result suggests that Eq. (10) can be applied to systems with the restitution coefficient ranging from 0.3 to 0.9.

IV. CONCLUSIONS

In this paper, discrete element method simulations of shear flow with the Lees-Edwards boundary condition are performed to quantify the relation between the diffusion coefficient and flow parameters for size bidisperse systems. Simulation results show that small particles diffuse faster than large particles in bidisperse mixtures. The average particle diameter weighted by particle volume is found to be appropriate for scaling the average diffusion coefficient in size bidisperse systems.

The simulation results indicate that the diffusion coefficient D is proportional to the shear rate $\dot{\gamma}$ and the square of the average particle diameter d^2 but inversely proportional to the solids fraction f in the dense flow regime and that the diameter ratio D_{LS} has minimal influence on the diffusion coefficient for $D_{LS} \leqslant 3{:}1$. The diffusion coefficient can be expressed as $D = k_d \dot{\gamma} d^2$, and the constant is quantitatively measured as $k_d = 0.0186/f$. This relation can be used in other dense granular flow with various shear rates $\dot{\gamma}$, solids fractions f, diameter ratios D_{LS}, and component ratios C_{LS}, and also can be applied to systems with the restitution coefficient e ranging from 0.3 to 0.9 and the friction coefficient μ ranging from 0.1 to 1. In simulations with $\mu < 0.1$, the diffusion coefficient increases significantly as μ decreases, which is possibly a consequence of reduced rotational particle motion.

Different from previous studies, no arbitrary fitting parameters are required for calculating the diffusion coefficient with this approach, and the scaling can be integrated into continuum models. In this approach, the shear rate and the solids fraction are well controlled for each simulation case. There is no gravity and the measurement of the diffusion coefficient is not influenced by the gravity-driven segregation phenomenon. Therefore, the quantified relation can be used in other flows with bidisperse spheres such as tumbler flow, chute flow, and heap flow with size bidisperse spheres. An example for its application in bounded heap flow is shown in the Appendix.

The unresolved phenomena found in this paper should be of interest for future studies. Specifically, a better understanding of the difference of the diffusion coefficient for individual species in a size bidisperse mixture can possibly lead to more insight into modeling segregation. The increase of the diffusion coefficient with the particle friction smaller than 0.1, and the possible deviation of the diffusion behavior from the scaling for the particle diameter ratio larger than 3, should also be investigated. Furthermore, it is also worthwhile to consider quantifying the diffusion of nonspherical particles, as the particle shape and the diffusion can be coupled [42].

APPENDIX: APPLICATIONS IN BOUNDED HEAP FLOW

The relation for diffusion of size bidisperse spheres in dense flow, $D = k_d \dot{\gamma} d^2$, is applied to modeling segregation in bounded heap flows in this Appendix. DEM simulations are used to study the segregation of size bidisperse spheres in a quasi-2D one-sided bounded heap, which is a canonical geometry for studying granular segregation [2,14,55,56]. Following previous studies [42,56], in our simulation of quasi-2D bounded heap flow, the container is empty initially and size bidisperse mixtures are fed by gravity at the left end of the container. The particles flow downstream and form a quasi-2D bounded heap, during which size segregation occurs.

We apply a continuum model that has been successfully used for quantitatively predicting size bidisperse segregation in different geometries [4,5,41,49,57,58], as well as density bidisperse segregation [35]. This continuum segregation model is based on a modified transport equation:

$$\frac{\partial c_i}{\partial t} + \nabla \cdot (\boldsymbol{u} c_i) + \frac{\partial}{\partial z}(w_{s,i} c_i) - \nabla \cdot (D \nabla c_i) = 0, \quad \text{(A1)}$$

where c_i is the concentration of species i (l for large and s for small) such that $c_i = f_i/f$, where f_i is the local volume fraction of species i, and f is the total volume fraction for all species. Equation (A1), which includes the interplay of advection, segregation, and diffusion, is applied to the thin flowing layer (with length L and depth δ) near the free surface of the heap where segregation occurs. In the flowing layer, x denotes the streamwise direction ($0 < x < L$), and z denotes the depthwise direction ($-\delta < z < 0$), with $z = 0$ at the flowing layer surface and $z = -\delta$ at the bottom of the flowing layer. The average 2D velocity field is $\boldsymbol{u} = u\boldsymbol{x} + w\boldsymbol{z}$, and D denotes the diffusion coefficient (variables without subscripts represent the average flow properties of both particle species). A crucial part of this model is the segregation velocity $w_{s,i}$, which is the relative normal velocity of species i with respect to the normal velocity of both species: $w_{s,i} = w_i - w$. To solve this model, kinematic information including the 2D average velocity field, the segregation velocity, and the diffusion coefficient is required. The diffusion coefficient is expressed by Eq. (10) and the segregation velocity is calculated according to Eqs. (3.2a) and (3.2b) in Ref. [5], while the velocity field can also be calculated by scalings in Ref. [5].

To demonstrate that the relation of the diffusion coefficient with $k_D = 0.0186$ can be applied to accurately predicting size bidisperse segregation in the quasi-2D bounded heap, three groups of theoretical predictions and simulation results for the concentration of the small particles at the bottom of the flowing layer for different diameter ratios D_{LS} and feed rate $q = 14.048 \text{ cm}^2/\text{s}$ are shown in Fig. 12. The quasi-2D bounded heap has width $W = 0.69 \text{ m}$ and gap thickness $T = 0.032 \text{ m}$ with four kinds of particle diameters: 2, 3, 4, and 6 mm. To save computation time, the bottom wall is inclined as the effect of the bottom wall can be neglected, which is validated in our previous study [42]. As shown in Fig. 12, it is clear that the theoretical model reproduces the segregation patterns in simulations with good accuracy, demonstrating that the quantified relation can be well applied to the bounded heap flow.
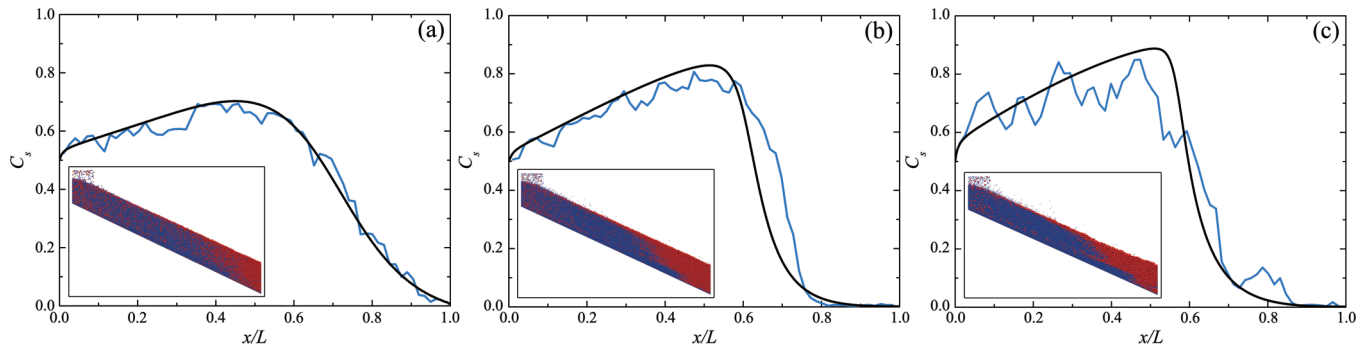
FIG. 12. Comparisons between theoretical predictions and simulation results for size bidisperse segregation with different diameter ratios D_{LS} when feed rate $q = 14.048\,\mathrm{cm^2/s}$ and solids fraction $f = 59\%$ (average f measured from simulations): $D_{LS} = 4{:}3$ mm in (a), $D_{LS} = 4{:}2$ mm in (b) and $D_{LS} = 6{:}2$ mm in (c). Theoretical predictions (black curves) and simulation results (blue curves) for the concentration of the small particles at the bottom of the flowing layer for different D_{LS} are in (a), (b) and (c). Blue and red spheres represent small and large spheres, respectively, in the insets of (a), (b) and (c) .

[1] J. Choi, A. Kudrolli, R. R. Rosales, and M. Z. Bazant, Phys. Rev. Lett. **92**, 174301 (2004).

[2] Y. Fan, Y. Boukerkour, T. Blanc, P. B. Umbanhowar, J. M. Ottino, and R. M. Lueptow, Phys. Rev. E **86**, 051305 (2012).

[3] A. Tripathi and D. V. Khakhar, J. Fluid Mech. **717**, 643 (2013).

[4] Y. Fan, C. P. Schlick, P. B. Umbanhowar, J. M. Ottino, and R. M. Lueptow, J. Fluid Mech. **741**, 252 (2014).

[5] C. P. Schlick, Y. Fan, P. B. Umbanhowar, J. M. Ottino, and R. M. Lueptow, J. Fluid Mech. **765**, 632 (2015).

[6] G. Marty and O. Dauchot, Phys. Rev. Lett. **94**, 015701 (2005).

[7] J. D. Seymour, A. Caprihan, S. A. Altobelli, and E. Fukushima, Phys. Rev. Lett. **84**, 266 (2000).

[8] N. Jain, J. M. Ottino, and R. M. Lueptow, Phys. Fluids **14**, 572 (2002).

[9] K. M. Hill, G. Gioia, and V. V. Tota, Phys. Rev. Lett. **91**, 064302 (2003).

[10] S. W. Meier, R. M. Lueptow, and J. M. Ottino, Adv. Phys. **56**, 757 (2007).

[11] S. B. Savage and C. K. K. Lun, J. Fluid Mech. **189**, 311 (1988).

[12] N. Menon and D. J. Durian, Science **275**, 1920 (1997).

[13] S. Wiederseiner, N. Andreini, G. Épelychauvin, G. Moser, M. Monnereau, J. M. N. T. Gray, and C. Ancey, Phys. Fluids **23**, 013301 (2011).

[14] Y. Fan, P. B. Umbanhowar, J. M. Ottino, and R. M. Lueptow, Proc. R. Soc. A. **469**, 20130235 (2013).

[15] J. Baxter, U. Tüzün, D. Heyes, I. Hayati, and P. Fredlund, Nature (London) **391**, 136 (1998).

[16] D. M. Mueth, G. F. Debregeas, G. S. Karczmar, P. J. Eng, S. R. Nagel, and H. M. Jaeger, Nature (London) **406**, 385 (2000).

[17] W. Losert, L. Bocquet, T. C. Lubensky, and J. P. Gollub, Phys. Rev. Lett. **85**, 1428 (2000).

[18] S. Luding, Particul. Sci. Technol. **26**, 33 (2007).

[19] S. B. Savage and R. Dai, Mech. Mater. **16**, 225 (1993).

[20] S. S. Hsiau and Y. M. Shieh, J. Rheol. **43**, 1049 (1999).

[21] S. S. Hsiau and W. L. Yang, Phys. Fluids **14**, 612 (2002).

[22] J. Bridgwater, Powder Technol. **25**, 129 (1980).

[23] C. S. Campbell, J. Fluid Mech. **348**, 85 (1997).

[24] C. S. Campbell, Powder Technol. **162**, 208 (2006).

[25] B. Utter and R. P. Behringer, Phys. Rev. E **69**, 031308 (2004).

[26] S. S. Hsiau and Y. M. Shieh, Chem. Eng. Sci. **55**, 1969 (2000).

[27] Y. Fan, P. B. Umbanhowar, J. M. Ottino, and R. M. Lueptow, Phys. Rev. Lett. **115**, 088001 (2015).

[28] S. S. Hsiau and M. L. Hunt, J. Heat Transfer **115**, 541 (1993).

[29] V. V. R. Natarajan, M. L. Hunt, and E. D. Taylor, J. Fluid Mech. **304**, 1 (1995).

[30] H. Katsuragi, A. R. Abate, and D. J. Durian, Soft Matter **6**, 3023 (2010).

[31] P. Kharel and P. Rognon, Phys. Rev. Lett. **119**, 178001 (2017).

[32] F. Radjai and S. Roux, Phys. Rev. Lett. **89**, 064302 (2002).

[33] V. Richefeu, G. Combe, and G. Viggiani, Géotechnique Lett. **2**, 113 (2012).

[34] G. Combe, V. Richefeu, M. Stasiak, and A. P. F. Atman, Phys. Rev. Lett. **115**, 238301 (2015).

[35] H. Xiao, P. B. Umbanhowar, J. M. Ottino, and R. M. Lueptow, Proc. R. Soc. A. **472**, 20150856 (2016).

[36] J. M. N. T. Gray and V. A. Chugunov, J. Fluid Mech. **569**, 365 (2006).

[37] J. M. N. T. Gray and A. R. Thornton, Proc. R. Soc. A. **461**, 1447 (2005).

[38] J. M. N. T. Gray and C. Ancey, J. Fluid Mech. **678**, 535 (2011).

[39] M. Benjy, R. Pierre, and E. Itai, J. Fluid Mech. **690**, 499 (2012).

[40] A. Thornton, T. Weinhart, S. Luding, and O. Bokhove, Int. J. Mod. Phys. C **23**, 1240014 (2012).

[41] C. P. Schlick, Y. Fan, A. B. Isner, P. B. Umbanhowar, J. M. Ottino, and R. M. Lueptow, AIChE J. **61**, 1524 (2015).

[42] Y. Zhao, H. Xiao, P. B. Umbanhowar, and R. M. Lueptow, AIChE J. **64**, 1550 (2018).

[43] A. W. Lees and S. F. Edwards, J. Phys. C **5**, 1921 (1972).

[44] P. A. Cundall and O. D. L. Strack, Géotechnique **29**, 47 (1979).

[45] J. M. Ting and B. T. Corkum, J. Comput. Civ. Eng. **6**, 129 (1992).

[46] H. Ma, L. Xu, and Y. Zhao, Powder Technol. **314**, 355 (2017).

[47] Y. You, M. Liu, H. Ma, L. Xu, B. Liu, Y. Shao, Y. Tang, and Y. Zhao, Powder Technol. **325**, 316 (2017).

[48] A. S. Keys, A. R. Abate, S. C. Glotzer, and D. J. Durian, Nat. Phys. **3**, 260 (2007).

[49] R. P. Jones, A. B. Isner, H. Xiao, J. M. Ottino, P. B. Umbanhowar, and R. M. Lueptow, Phys. Rev. Fluids **3**, 094304 (2018).

[50] K. van der Vaart, P. Gajjar, G. Epely-Chauvin, N. Andreini, J. M. N. T. Gray, and C. Ancey, Phys. Rev. Lett. **114**, 238001 (2015).

[51] A. Tripathi and D. V. Khakhara, Phys. Fluids, **23**, 113302 (2011).

[52] A. M. Fry, P. B. Umbanhowar, J. M. Ottino, and R. M. Lueptow, AIChE J. **65**, 875 (2019).

[53] L. Jing, C. Y. Kwok, and Y. F. Leung, Phys. Rev. Lett. **118**, 118001 (2017).

[54] B. Kou, Y. Cao, J. Li, C. Xia, Z. Li, H. Dong, A. Zhang, J. Zhang, W. Kob, and Y. Wang, Phys. Rev. Lett. **121**, 018002 (2018).

[55] Y. Fan, K. V. Jacob, B. Freireich, and R. M. Lueptow, Powder Technol. **312**, 67 (2017).

[56] H. Xiao, D. McDonald, Y. Fan, P. B. Umbanhowar, J. M. Ottino, and R. M. Lueptow, Powder Technol. **312**, 360 (2017).

[57] C. P. Schlick, A. B. Isner, P. B. Umbanhowar, R. M. Lueptow, and J. M. Ottino, Ind. Eng. Chem. Res. **54**, 10465 (2015).

[58] H. Xiao, Y. Fan, K. V. Jacob, P. B. Umbanhowar, M. Kodam, J. F. Koch, and R. M. Lueptow, Chem. Eng. Sci. **193**, 188 (2019).